

## Research Article

# Aerodynamic Optimization of an Over-the-Wing-Nacelle-Mount Configuration

**Daisuke Sasaki and Kazuhiro Nakahashi**

*Department of Aerospace Engineering, Tohoku University, Aoba 6-6-01, Sendai 980-8579, Japan*

Correspondence should be addressed to Daisuke Sasaki, [sasaki@ad.mech.tohoku.ac.jp](mailto:sasaki@ad.mech.tohoku.ac.jp)

Received 14 November 2010; Revised 21 February 2011; Accepted 21 February 2011

Academic Editor: Guan Yeoh

Copyright © 2011 D. Sasaki and K. Nakahashi. This is an open access article distributed under the Creative Commons Attribution License, which permits unrestricted use, distribution, and reproduction in any medium, provided the original work is properly cited.

An over-the-wing-nacelle-mount airplane configuration is known to prevent the noise propagation from jet engines toward ground. However, the configuration is assumed to have low aerodynamic efficiency due to the aerodynamic interference effect between a wing and a nacelle. In this paper, aerodynamic design optimization is conducted to improve aerodynamic efficiency to be equivalent to conventional under-the-wing-nacelle-mount configuration. The nacelle and wing geometry are modified to achieve high lift-to-drag ratio, and the optimal geometry is compared with a conventional configuration. Pylon shape is also modified to reduce aerodynamic interference effect. The final wing-fuselage-nacelle model is compared with the DLR F6 model to discuss the potential of Over-the-Wing-Nacelle-Mount geometry for an environmental-friendly future aircraft.

## 1. Introduction

With the growth in aircraft traffic, there is a strong demand to reduce the airport noise. The major sources of the airport noise are jet and fan noises caused by the engine. All over the world, regulations on airport noise have been tightened, thus it is a significant problem to reduce airframe and engine noises.

To reduce the airport noise, several aircraft configurations have been proposed lately. One is to install engine nacelles over the aft fuselage, and another is to install engine nacelles over the wing. In the latter case, successful experiences are only a few cases including the recent Honda Business jet [1]. The Over-the-Wing-Nacelle (OWN) configuration has a potential to reduce the noise drastically because the wing can block the propagation of fan and jet noises toward ground [2]. However, when the engine nacelles are installed over the wing, the aerodynamic performance tends to drop significantly due to the interference effect. If the interference effect between a nacelle and a wing is weakened and large increase in aerodynamic performance is achieved, OWN configuration will be a potential candidate to be a near-future quiet aircraft configuration.

Therefore, the purpose of this study is to investigate the aerodynamic feasibility of OWN configuration by making use of computational fluid dynamics (CFD) and optimization methods. The cruise Mach number is set to 0.70 to focus on mid-sized, short-range aircraft for the Japanese domestic or European use. In this study, aerodynamic interference effect between a nacelle and a wing is optimized through the modification of nacelle, wing, and pylon shapes. The Kriging model is adopted to build an approximation model of the objective functions to reduce the large computational burden demanded by a stochastic optimization method coupled with 3D high-fidelity CFD computation around a full aircraft geometry.

## 2. Optimization Method

In aerodynamic shape optimizations, nonlinearity of the objective functions must be taken into consideration. Therefore, stochastic optimization methods are required to obtain global optimal solutions. Genetic algorithms (GA) is one of the popular stochastic methods often used for aerodynamic optimizations [3, 4]. GA is a population-based optimization method simulating the evolutionary process of creatures,

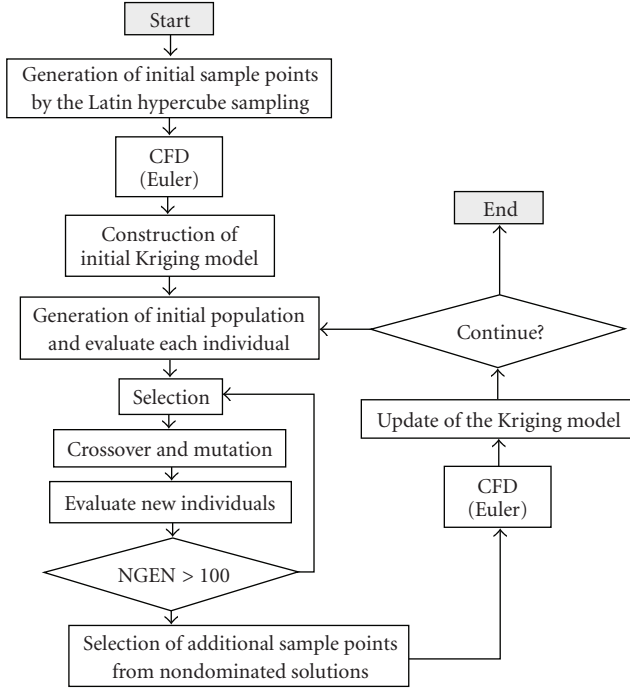


FIGURE 1: Flowchart of aerodynamic design system.

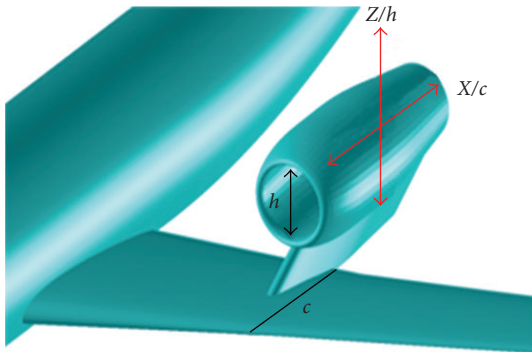
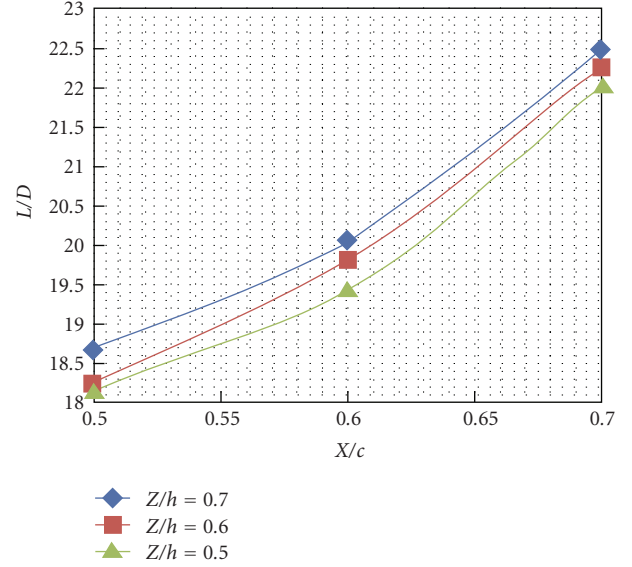


FIGURE 2: Definition of nacelle position.

in which the population evolves over generations to minimize/maximize the objective functions with the operations of selection, crossover, and mutation. In this research, an in-house solver of real-coded GA is adopted [3]. However, it is well-known that GA requires large computational cost due to population-based search, particularly coupled with expensive CFD solvers.

Therefore, surrogate model is used to approximate objective function values, which enables to prevent large number of expensive CFD evaluations and accelerate optimization procedure. Many surrogate models are proposed, but the Kriging model [5, 6] is adopted as it can predict nonlinear objective functions accurately. The Kriging model expresses the unknown function as sum of constant global model and local deviation from the global model. The surrogate model is built from the sampling points, where  $i$ th sampling point's

FIGURE 3:  $L/D$  with different nacelle position.

objective function value is  $y^i$  with the design variable vector of  $\mathbf{x}^i$ . Here, the number of sampling points is set to  $n$ , and the design vector size is set to  $k$ .

In the Kriging model, the predictor  $\hat{y}$  is represented to satisfy the following relation of correlation between real function value  $y$  of sampling points and the predictor  $\hat{y}$ :

$$\text{cor}(y(\mathbf{x}^i), \hat{y}(\mathbf{x})) = \psi^i = \exp\left(-\sum_{j=1}^k \theta_j |x_j^i - x_j|^2\right), \quad (1)$$

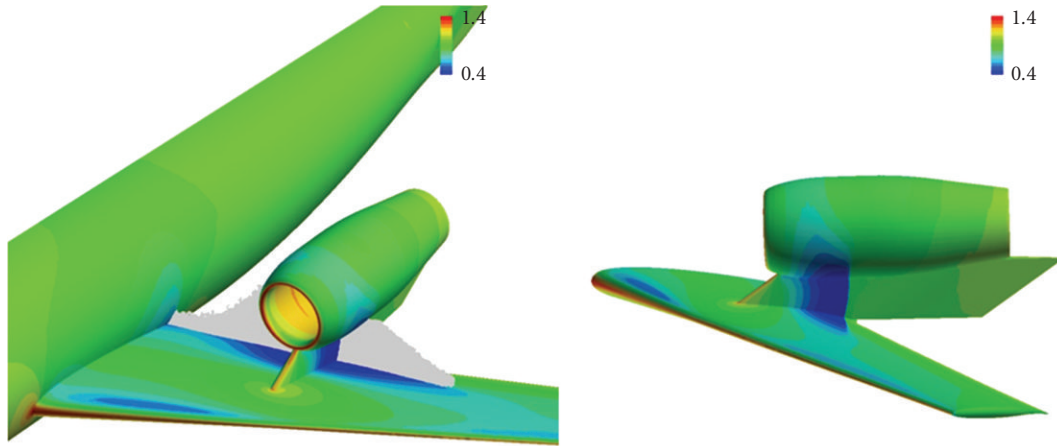
where  $\mathbf{x}$  is design variable vector of unknown objective function,  $x_j^i$  is  $j$ th design variable of  $i$ th sampling point, and  $x_j$  is  $j$ th design variable for the prediction. The correlation vector parameter  $\theta_j$  in (1) is the key of the Kriging model, and the best parameter needs to be obtained. The Kriging predictor is defined as

$$\hat{y}(\mathbf{x}) = \hat{\mu} + {}^t \boldsymbol{\psi} \boldsymbol{\Psi}^{-1} (\mathbf{y} - \mathbf{1} \hat{\mu}), \quad (2)$$

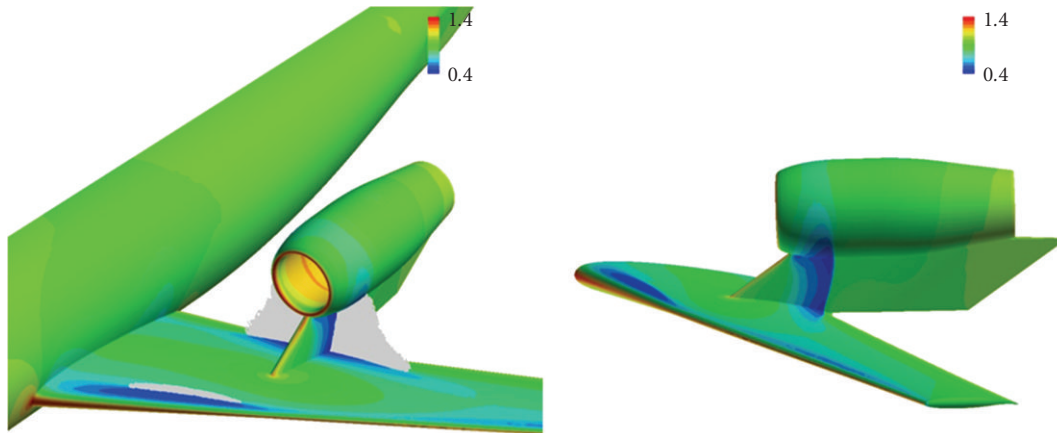
where  $\hat{\mu}$  is the estimated value of  $\mu$ ,  $\boldsymbol{\Psi}$  denotes  $n \times n$  correlation matrix whose  $(i, j)$  entry is correlation between the sampling points  $x^i$  and  $x^j$ , and  $\mathbf{1}$  is  $n$ -dimensional unit vector;

$$\hat{\mu} = \frac{{}^t \mathbf{1} \boldsymbol{\Psi}^{-1} \mathbf{y}}{{}^t \mathbf{1} \boldsymbol{\Psi}^{-1} \mathbf{1}}, \quad (3)$$

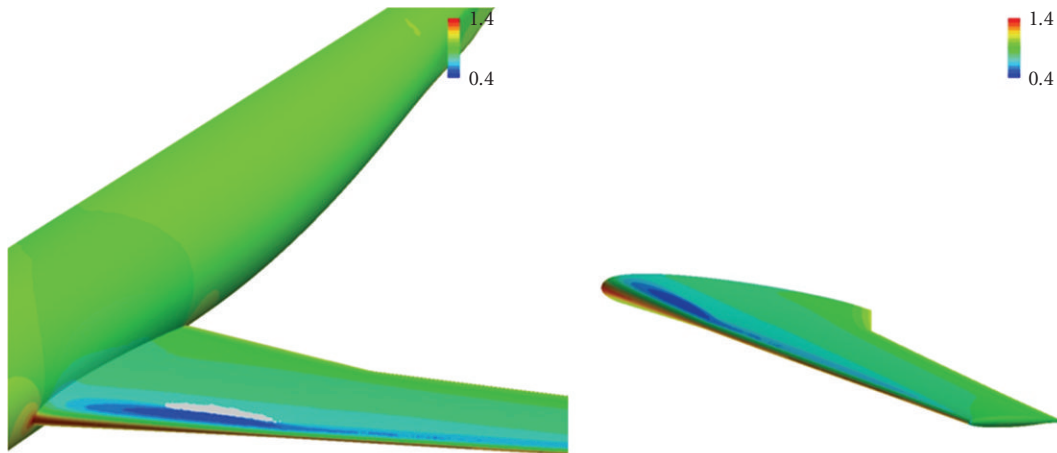
$$\sigma^2 = \frac{{}^t (\mathbf{y} - \mathbf{1} \hat{\mu}) \boldsymbol{\Psi}^{-1} (\mathbf{y} - \mathbf{1} \hat{\mu})}{n},$$



(a) Wing body with nacelle shape I ( $X/c = 0.50, Z/h = 0.5, L/D = 18.2$ )



(b) Wing body with nacelle shape II ( $X/c = 0.70, Z/h = 0.7, L/D = 22.5$ )



(c) Wing body without nacelle ( $L/D = 33.8$ )

FIGURE 4: Three wing body configurations with/without nacelle.

$\hat{\mu}$  and  $\sigma^2$  are used to specify the unknown parameter  $\theta$  by maximizing the following likelihood function:

$$\ln L \approx -\frac{n}{2} \ln \hat{\sigma}^2 - \frac{1}{2} \ln |\Psi|. \quad (4)$$

Here, GA is used to maximize the function to find the best parameter of  $\theta$  as it is  $k$ -dimensional unconstrained nonlinear problem. The Kriging model is then established, and the objective function is estimated using (2).

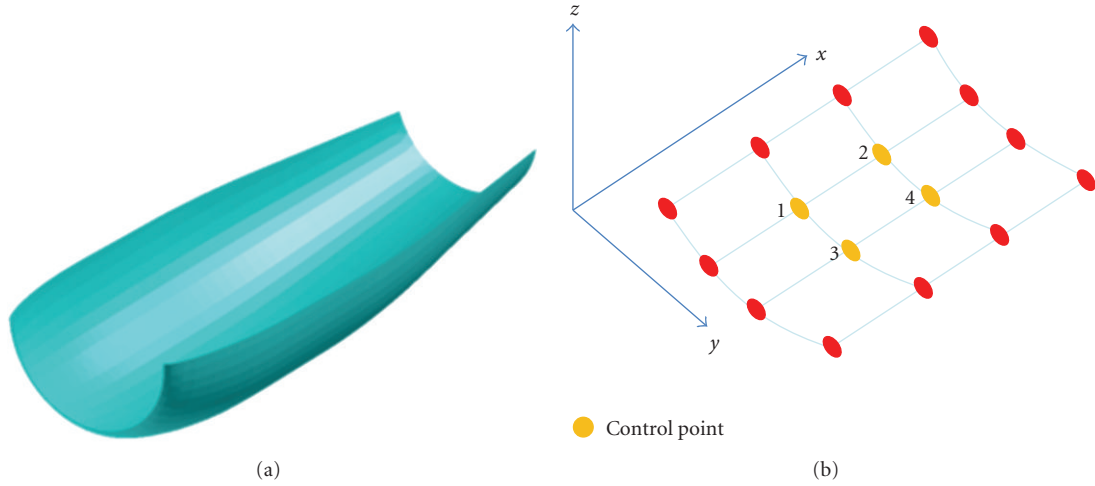


FIGURE 5: Nacelle lower shape definition.

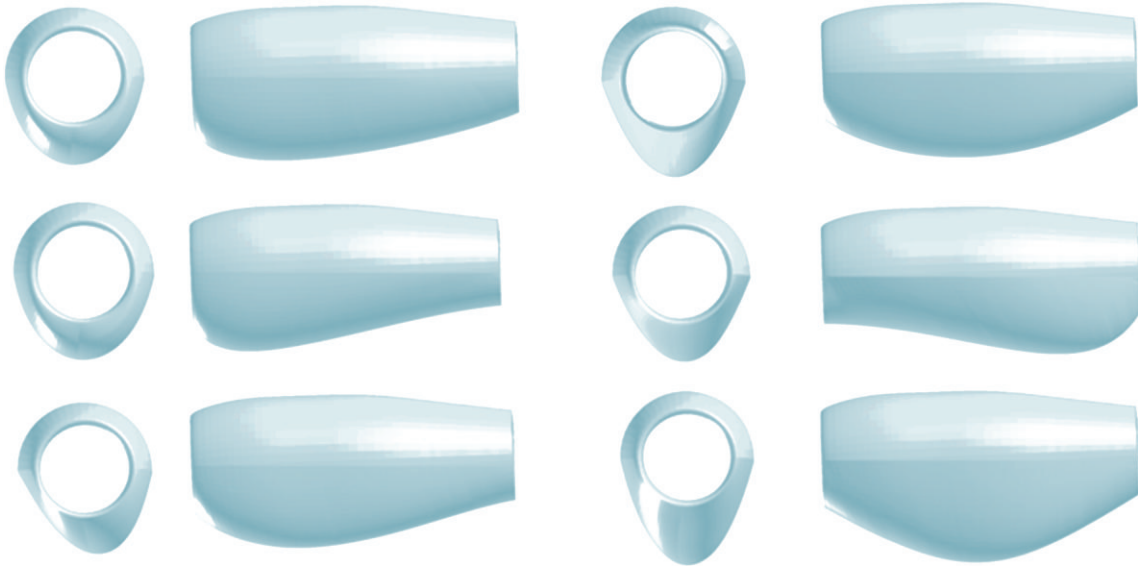


FIGURE 6: Examples of nacelle shape.

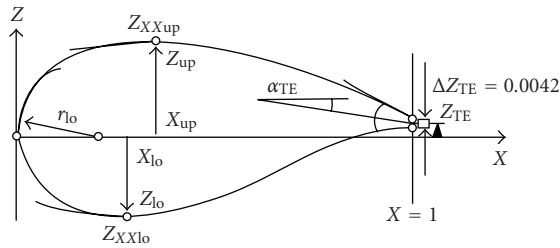


FIGURE 7: PARSEC airfoil definition.

One of advantages of the Kriging model is the capability to estimate the uncertainty of the estimated value. The mean square error  $s^2(\mathbf{x})$  at the point  $\mathbf{x}$  is expressed as

$$s^2(\mathbf{x}) = \hat{\sigma}^2 \left( 1 - \frac{\mathbf{t} \boldsymbol{\Psi} \boldsymbol{\Psi}^{-1} \boldsymbol{\psi}}{\mathbf{t} \mathbf{1} \boldsymbol{\Psi}^{-1} \mathbf{1}} + \frac{1 - \mathbf{t} \mathbf{1} \boldsymbol{\Psi}^{-1} \boldsymbol{\psi}}{\mathbf{t} \mathbf{1} \boldsymbol{\Psi}^{-1} \mathbf{1}} \right). \quad (5)$$

By integrating this with probability density function, the following so-called expected improvement (EI) value is obtained when minimization problem is considered:

$$EI(\mathbf{x}) = \int_{-\infty}^{y_{\text{opt}}} Y \frac{1}{s(\mathbf{x})\sqrt{2\pi}} \exp\left(-\frac{\{Y - \hat{y}(\mathbf{x})\}^2}{2s(\mathbf{x})^2}\right) dY, \quad (6)$$

where  $y_{\text{opt}}$  is the present optimal objective function value. The EI value represents the possible improvement at point  $\mathbf{x}$ . By using EI values, we can find design space where it is not explored yet but the objective function may be improved due to the high uncertainty.

In the present aerodynamic optimization, the above-mentioned Kriging approximate model is used to compute objective function values instead of CFD calculations. Here, the present Kriging model-based optimization procedure is described in Figure 1.

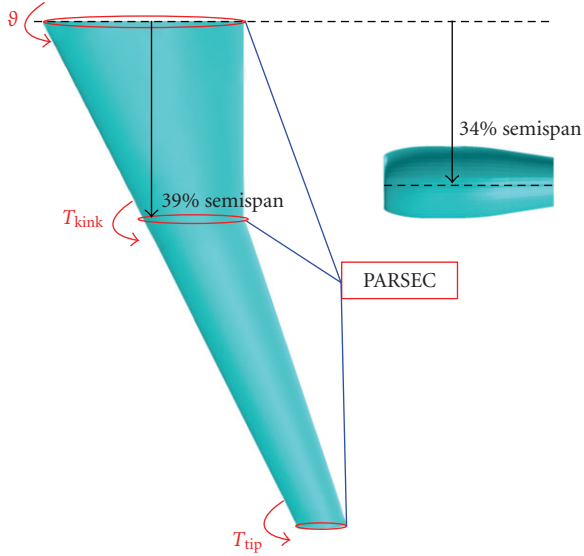


FIGURE 8: Planform shape, kink position, and nacelle location.

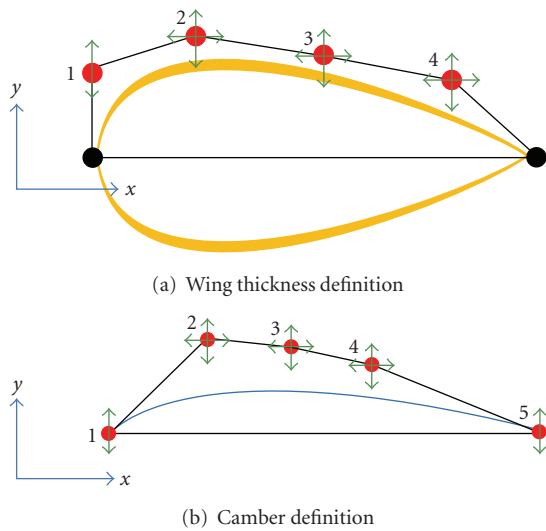


FIGURE 9: Pylon shape definition.

- (1) Select initial sampling points using the Latin hypercube sampling;
- (2) compute objective function value of sampling points;
- (3) build Kriging model for an objective function;
- (4a) minimize objective function on Kriging model using GA;
- (4b) maximize EI value using GA;
- (5) add optimal points with regard to objective (4a) or EI (4b) as additional sampling;
- (6) iterate item (2)–(5) until termination condition is met.

To build the reliable Kriging model, well-distributed sampling points are needed. The Latin hypercube sampling

(LHS) method [7], one of design of experiments, is used to distribute the points in equidistance space. It is computationally expensive to spread initial sampling points all over the domain densely to build the accurate Kriging model. Therefore, the adaptive Kriging model approach is employed, where the Kriging model is updated through the optimization process. After the optimization of GA coupled with the Kriging model, new sampling points are selected from optimal solutions to compute the updated Kriging model. This enables to improve the accuracy of the approximation to find global optimal solutions. In this study, EI values are also used for the optimization to obtain new sample points for the purpose of the robust search of global optimal solutions.

### 3. Preliminary Analysis

In this section, preliminary analyses are conducted to investigate the aerodynamic interference due to the existence of a nacelle above a wing at cruise conditions. The configuration is based on the DLR-F6 used in the Third AIAA Drag Prediction Workshop [8]. The DLR-F6 is a conventional under-the-wing-nacelle (UWN) configuration composed of fuselage, wing, nacelle, and pylon. The original design Mach number of the DLR-F6 configuration is 0.75. In this research, the flow condition is set to the Mach number of 0.70 to focus on mid-sized, short-range aircraft. The lift coefficient  $C_L$  was kept to 0.57 by adjusting the angle of attack. The numerical flow analysis is performed on wing-fuselage configuration with/without disjoint nacelles. Here, the flow-through nacelle is used because the validity of flow-through nacelle simulation was proved in [1].

The flow around nine different configurations was simulated by Euler solver for comparison. The nacelle height from the upper wing surface ( $Z/h$ ) and the distance from the leading edge ( $X/c$ ) in Figure 2 are changed, where  $h$  is nacelle inlet diameter and  $c$  is chord length at the pylon used for the normalization. The  $L/D$  values of nine different configurations are summarized in Figure 3. The graph represents that the aerodynamic performance is highly affected by the nacelle position. In addition, the existence of nacelle interrogates the performance badly since  $L/D$  of wing-fuselage without nacelle is 33.8. The pressure distributions of the two configurations with the nacelle and a configuration without the nacelle are shown in Figure 4. In the figures, the following shock function is used for the detection of the shock region:

$$f_{\text{shock}} = \frac{(\mathbf{u} \cdot \nabla P)}{(a|\nabla P|)}, \quad (7)$$

where  $\mathbf{u}$  is velocity vector,  $P$  is static pressure, and  $a$  is speed of sound. The gray region in the figure is the shock region. As shown in Figures 4(a) and 4(b) for the two OWN cases, generated shock waves between a wing and a nacelle are clearly observed. On the other hand, the shock region of the configuration without the nacelle is very small. These shock waves increase the drag and reduce the  $L/D$ . It concludes that OWN configuration tends to produce shock



FIGURE 10: Examples of pylon shapes.

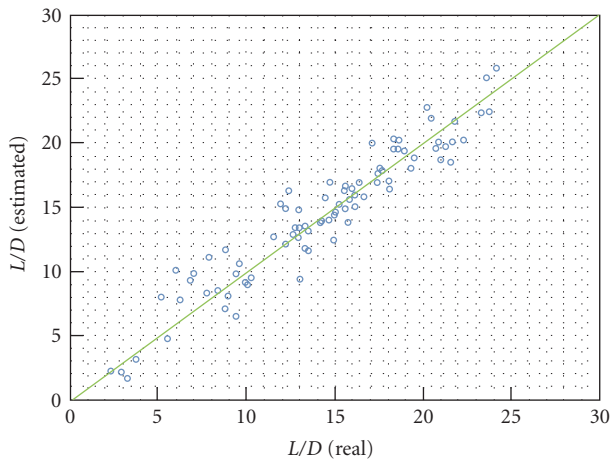


FIGURE 11: Cross-validation result of Kriging model built by first sampling points.

wave; however, the strength of shock waves strongly related to the position of engine nacelle installed. Therefore, by conducting the optimization of the nacelle position and the nacelle shape, aerodynamically feasible OWN configuration can be obtained.

#### 4. Problem Definition

In this paper, the objective is to improve aerodynamic performance of OWN configuration by modifying wing, nacelle, and pylon shapes. The first optimization is conducted to modify wing airfoil and nacelle shapes to reduce the aerodynamic interference effect between a wing and a nacelle. The optimal design is then further improved to optimize the pylon shape. Here, the optimization problem for the two cases is defined.

**4.1. Objective and Constraint.** The aim is to investigate the feasibility of aerodynamically efficient OWN configuration. When only the aerodynamic efficiency is considered, the

TABLE 1: Nacelle position range.

	Min	Max
$X/c$	0.47	0.85
$Z/h$	0.42	0.76

nacelle position tends to be away from the wing (higher and rearward). This causes the problem in maintainability and structure. Therefore, the consideration of structural and maintenance necessities is included in the optimization, geometric parameters of nacelle location as shown in Figure 2 are chosen to be optimized (lower and forward) as an incentive to more realistic design. The objectives and a constraint are summarized below.

Objectives:

- (1) maximize cruise  $L/D$ ,
- (2) minimize nacelle height ( $Z/h$ ),
- (3) minimize nacelle rearward location ( $X/c$ ).

Constraints:

- (1) constant  $C_L = 0.57$ .

The design is conducted under the cruise condition of Mach 0.70 with  $C_L$  of 0.57. This optimization problem is solved by GA coupled with Kriging approximation as described in Section 2.

**4.2. Nacelle Definition.** The nacelle position is defined by two design variables ( $X/c$ ,  $Z/h$ ) representing the front-rear and vertical movement as shown in Figure 3. The ranges of the variables are defined in Table 1.

The lower surface of nacelle is defined by Bezier surface of four by four control points shown in Figure 5. Bezier surface is controlled by the  $x$ ,  $y$ ,  $z$  coordinates of intermediate four control points, which correspond to 12 design variables ( $4 \times 3 = 12$  variables). The upper surface of nacelle is frozen to original DLR-F6 type [8]. Therefore, the designed lower

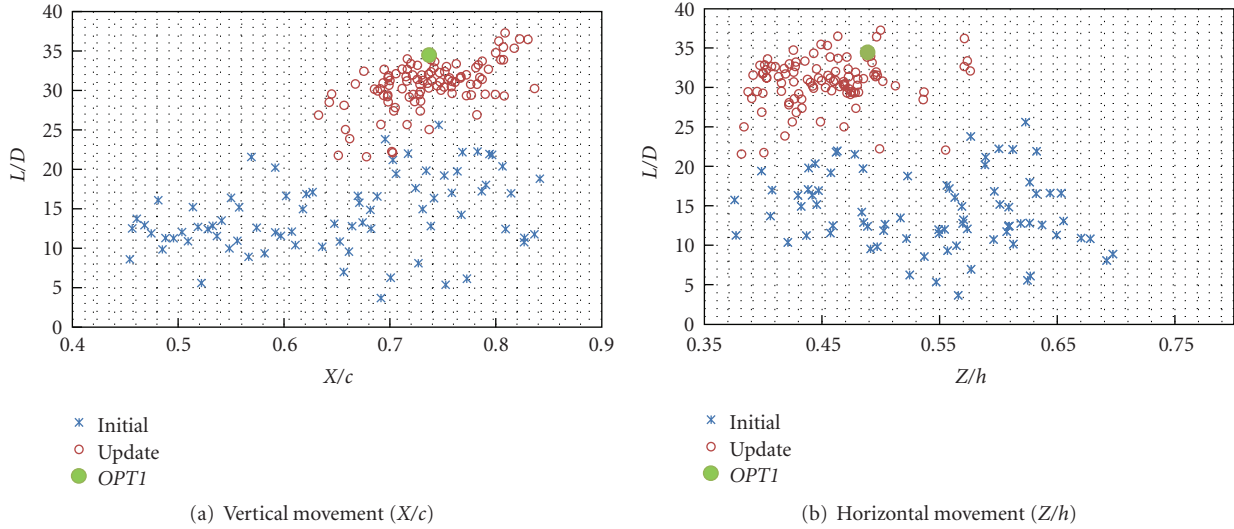


FIGURE 12:  $L/D$  distribution against nacelle position (blue: initial samples, red: update points).

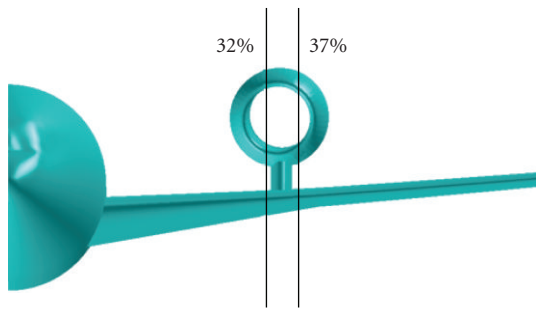


FIGURE 13: Cut planes at inner and outer nacelle.

nacelle surface is combined with the upper surface of DLR-F6's nacelle to define the whole nacelle. The examples of possible nacelle shape are represented in Figure 6.

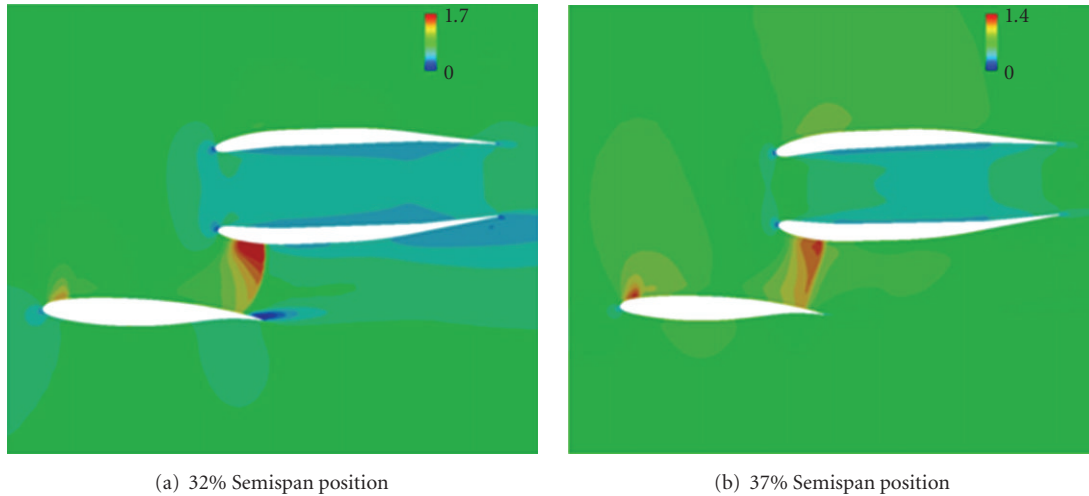
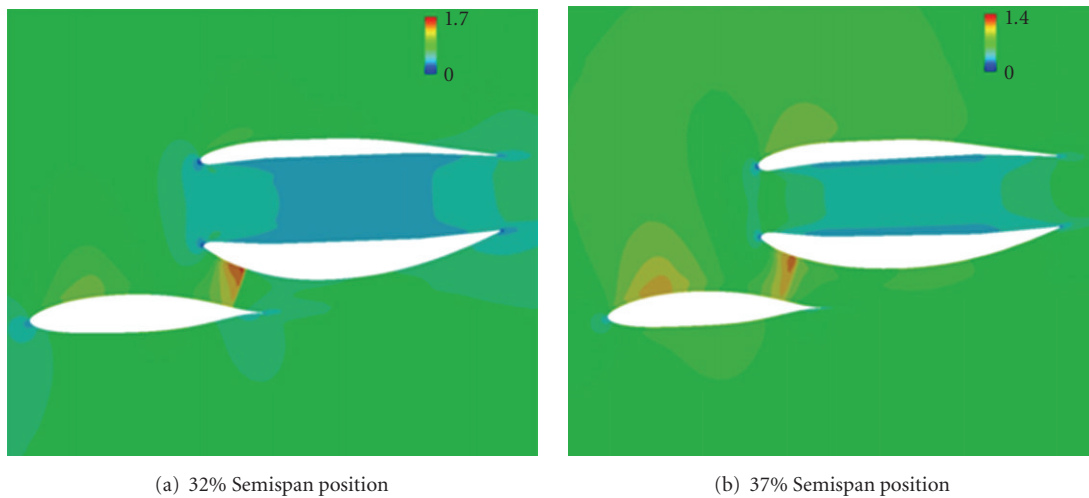
**4.3. Wing Definition.** The 3-D wing shape is defined by the following 30 design variables to control the airfoil shapes while the planform of the wing is frozen to original DLR-F6 type. The root, tip, and kink sectional airfoils are defined by nine design variables each according to the PARSEC definition [4, 9] as shown in Figure 7. The remaining sectional airfoils are linearly interpolated. In such parameterization, the complex shape of each airfoil can be represented by a relatively small number of meaningful engineering parameters such as the crest of the upper surface's  $Z$  coordinate ( $Z_{up}$ ), the crest of the lower surface's  $Z$  coordinate ( $Z_{lo}$ ) and the leading edge radius ( $r_{LE}$ ). This engineering parameterization is useful for designers to analyze optimized data directly. In addition, the wash-out is defined by two design variables at tip and kink position ( $T_{kink}$ ,  $T_{tip}$ ). Furthermore, the incidence angle ( $\theta$ ) is defined at root position. The planform with the design (kink) section is shown in Figure 8, and the ranges of design parameters are summarized in Table 2.

TABLE 2: Range of design parameters for PARSEC airfoil and twist Angles.

Parameter	Min	Max
$r_{le}$	0.005	0.06
$Z_{Te}$	-0.015	0.015
$\alpha_{Te}$	-8 deg.	-3 deg.
$X_{up}$	0.35	0.50
$Z_{up}$	0.06	0.13
$Z_{xxup}$	-1.0	-0.2
$X_{lo}$	0.35	0.5
$Z_{lo}$	-0.13	-0.06
$Z_{xxlo}$	0.1	1.0
Washout at tip	-4 deg.	4 deg.
Washout at kink	-4 deg.	4 deg.
Incidence angle (root)	0 deg.	8 deg.

**4.4. Pylon Definition.** The wing thickness of the pylon is defined by Bezier curve of four control points shown in Figure 9(a). There are seven design variables to control the wing thickness of the pylon. By using this geometrical definition, symmetrical airfoil of the pylon is represented. In addition, the camber is defined by Bezier curve of five control points shown in Figure 9(b). The camber is controlled by the  $x$ ,  $y$  coordinates of four control points, which correspond to eight design variables. Finally, a new pylon shape is generated by combining the wing thickness of the pylon with the camber. Therefore, 15 design variables are used in total. The possible pylon shapes are shown in Figure 10.

**4.5. Flow Analysis.** Once a new wing-fuselage-nacelle shape is defined, new surface mesh is firstly generated based on the advancing front method [10]. The tetrahedral volume mesh is then generated using Delaunay approach [11].

FIGURE 14:  $C_p$  distribution of *original* Geometry.FIGURE 15:  $C_p$  distribution of OPT1 geometry.

Qualitative volume mesh for a new wing-fuselage-pylon-nacelle configuration is always generated with the number of nodes around 1.3 million.

In this research, a wing-fuselage configuration with a nacelle and a pylon is analyzed using three-dimensional unstructured mesh CFD solver, TAS (Tohoku University Aerodynamic Simulation) code [12]. The compressible Euler equations are solved by a finite-volume cell-vertex scheme. The numerical flux normal to the control volume boundary is computed using an approximate Riemann solver of Harten-Lax-van Leer-Einfeldt-Wada (HLLEW) [13]. The second-order spatial accuracy is realized by a linear reconstruction of the primitive gas dynamic variables inside the control volume with Venkatakrishnan's limiter [14]. The LU-SGS implicit method for unstructured meshes [15] is used for the time integration. The accuracy of the TAS-code has been validated for various flow problems [4, 12].

## 5. Optimization Results

**5.1. Wing and Nacelle Optimization.** In the first optimization, the nacelle position and shape in Section 4.2 and wing shape in Section 4.3 are modified to improve aerodynamic performance. The configuration is defined by 44 design variables. The pylon shape is fixed to NASA SC(2)-0008 airfoil. Horizontal and vertical tails are not modelled as they do not affect the whole aerodynamic performance.

The first Kriging model was constructed using 79 initial sampling points of the Latin hypercube sampling. The cross-validation of this model is shown in Figure 11, and it indicates that a reasonable approximation model was constructed. The final Kriging model was constructed with 169 sample points in total after 12 updates. Several non-dominated solutions on the approximate model were chosen at each update to increase accuracy of the approximation toward optimal solutions.

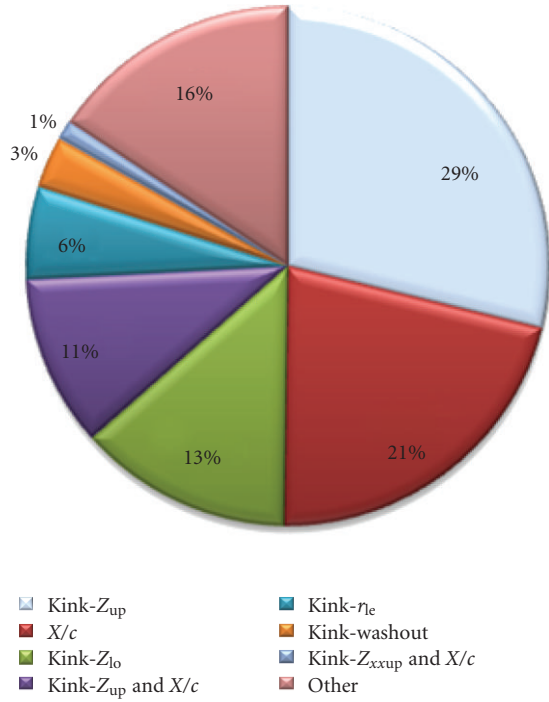


FIGURE 16: ANOVA result.

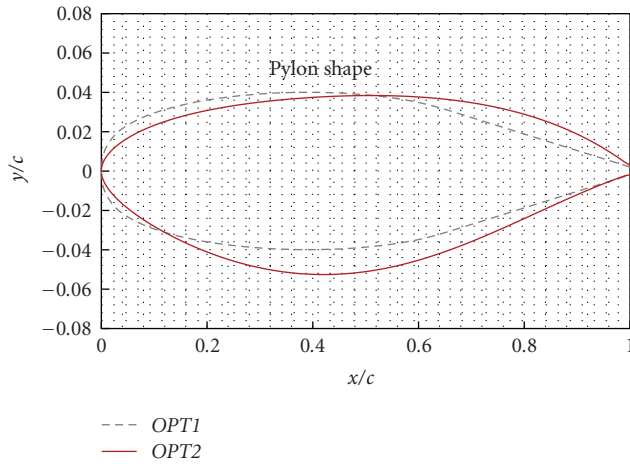


FIGURE 17: Comparison of pylon shape (blue: SC(2)-0008, red: OPT2).

Figure 12 shows objective-function space, which means the relation between  $L/D$  and nacelle position parameters. Due to the introduction of subobjectives ( $X/c$  and  $Z/h$ ), optimizer found higher  $L/D$  configurations at the nacelle position forward (low  $X/c$ ) and lower height (low  $Z/h$ ). One configuration having low  $X/c$  and  $Z/h$  parameters is chosen from non-dominated solutions ( $OPT1$ ), whose nacelle position parameters are  $X/c$  of 0.73 and  $Z/h$  of 0.48. This configuration achieved  $L/D$  of 34.5 at adjusted angle of attack of 5.71 degrees.

Mach number distributions of *ORIGINAL* ( $L/D$  of 25.0) and  $OPT1$  geometries at 32% and 37% semispan locations (viewed in Figure 13) are shown in Figures 14 and 15,

 TABLE 3: Pylon thickness and  $L/D$  for two optimal solutions ( $OPT1$  and  $OPT2$ ).

	$OPT1$	$OPT2$
Pylon thickness	8.0%	9.0%
$L/D$	34.5	35.5

respectively. From these figures, the shock wave of the  $OPT1$  is much weaker than that of the *ORIGINAL* because the flow channel between a wing and a nacelle is optimized to reduce interference effect. This is mainly due to the modification of lower nacelle shape.

To investigate the influence of each design variable to the objective function of  $L/D$ , ANOVA (functional analysis of variance) is conducted to the results. The result is shown in Figure 16, where the important design variables are shown in the figure. Many design variables related to the airfoil shape at the kink position are listed. Because the nacelle position is close to the kink position, the modification of the airfoil at the kink highly affects the flow between a nacelle and a wing.  $Z_{up}$ ,  $Z_{lo}$ ,  $r_{le}$  are the influenced factors and these three parameters are directly related to leading edge shape, which change the flow acceleration toward the nacelle.

**5.2. Pylon Optimization.** In the first optimization, wing and nacelle shapes are modified to improve aerodynamic efficiency. Here, further reduction of interference effect between a wing and a nacelle is intended by optimizing a pylon shape. In this section, the nacelle position and shape, and wing shape are frozen to the previous optimal geometry ( $OPT1$  configuration), and only the pylon is designed to be improved. The number of design variables is reduced to 15 in this case.

The first Kriging model was constructed using 41 sampling points of the Latin hypercube sampling, and the final Kriging model was constructed with 79 sample points in total after five updates.

The optimal design  $OPT2$  was obtained after the optimization and  $L/D$  of 35.4 was achieved at the angle of attack of 5.85 degrees. The results of  $OPT1$  and  $OPT2$  geometries are described in Table 3. The difference of  $L/D$  is tiny but  $OPT2$  actually achieved 5 counts drag reduction compared to  $OPT1$ . The modified pylon shapes are plotted in Figure 17. While the original SC (2)-0008 is symmetry, the designed pylon has camber and different leading edge radius, where positive  $y/c$  is inboard wing side and negative  $y/c$  is outboard wing side. In Figure 18, Mach contours of  $OPT1$  and  $OPT2$  are shown. According to the result, the  $OPT2$  reduces inboard shock waves due to the sharp leading edge and camber which enables to avoid flow acceleration between a wing and a nacelle. Pressure coefficient distributions at 32% and 37% semispan location are also plotted in Figure 19. This also indicates that inboard shock wave is weakened due to the pylon shape modification.

The pressure drag of the  $OPT1$  and the  $OPT2$  is shown in Figure 20. It indicates that optimization of the pylon shape is contributed to reduce the drag of inboard wing. On the other hand, the thrust of pylon is slightly weaker because the shock

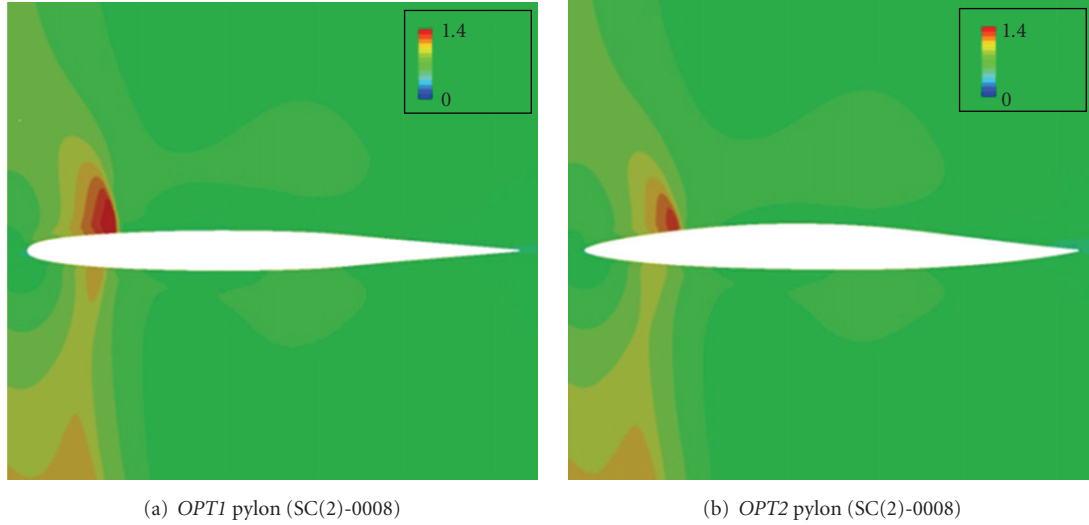
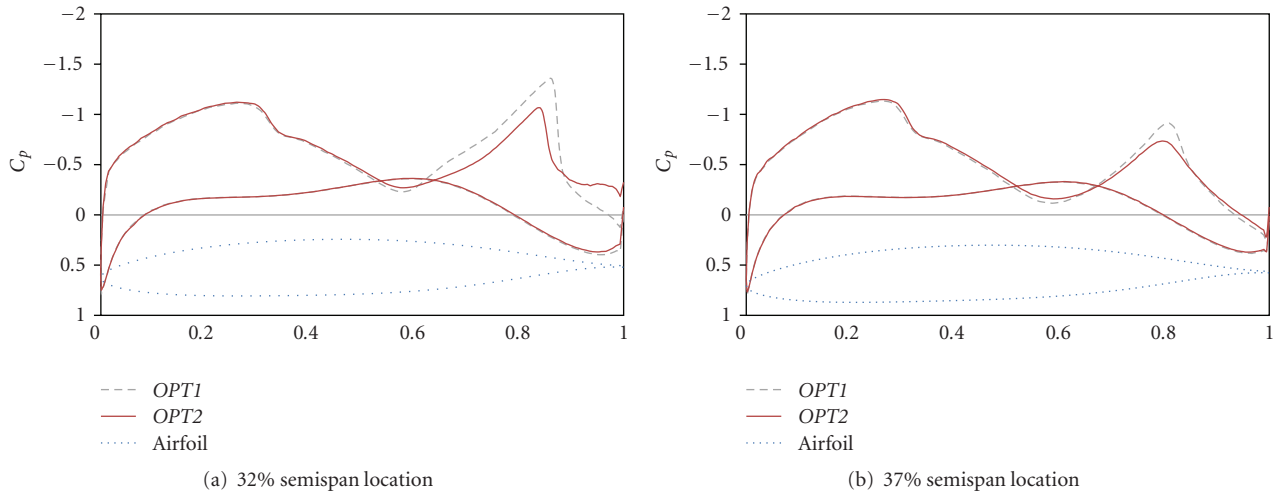


FIGURE 18: Comparison of Mach contours.

FIGURE 19: Comparison of  $C_p$  distribution (black line: *OPT1*, red line: *OPT2*).

wave near the leading edge of pylon is reduced by the pylon shape optimization.

**5.3. Performance of OWN Configuration.** The feasibility of OWN configuration is discussed herein through the comparison with DLR-F6 configuration that is conventional UWN configuration. The original design Mach number of DLR-F6 is 0.75. However, the Mach number in this research is set to 0.70 to focus on a mid-sized, short-range aircraft. Though they are not fully fair comparisons, the cruise performances of DLR-F6 and optimized OWN based on the *OPT2* at Mach number of 0.70 are compared in this section to investigate the aerodynamic feasibility of OWN configuration.

Surface pressure coefficient contours of both DLR-F6 and OWN configurations are shown in Figure 21. The aerodynamic performances are summarized in Table 4, and pressure drag components are plotted in Figure 22. From

TABLE 4: Cruise performance of DLR-F6 and OWN (*OPT2*) Configurations.

	DLR-F6	OWN ( <i>OPT2</i> )
$L/D$	31.7	35.5

this result, it demonstrates that optimized OWN configuration is able to achieve higher  $L/D$  than that of DLR-F6 configuration. This proves that OWN configuration has a potential to achieve high  $L/D$  comparable to conventional UWN by applying optimization techniques. When OWN configuration is realized, it is expected that the length of a landing gear can be much shortened compared to that of UWN configuration. This enables to reduce the total weight of the aircraft, which also leads to the increase of aerodynamic performance. In addition, as mentioned above, OWN configuration has an advantage of a shielding

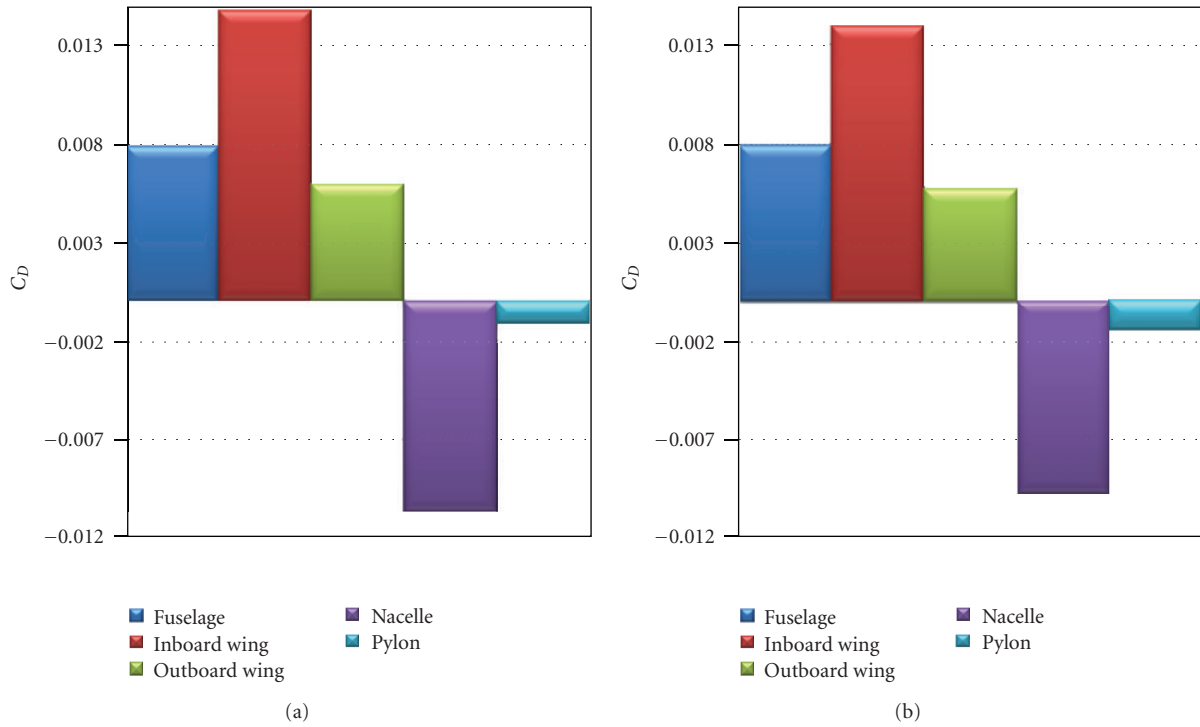


FIGURE 20: Proportion of pressure drag coefficient ((a) *OPT1*, (b) *OPT2*).

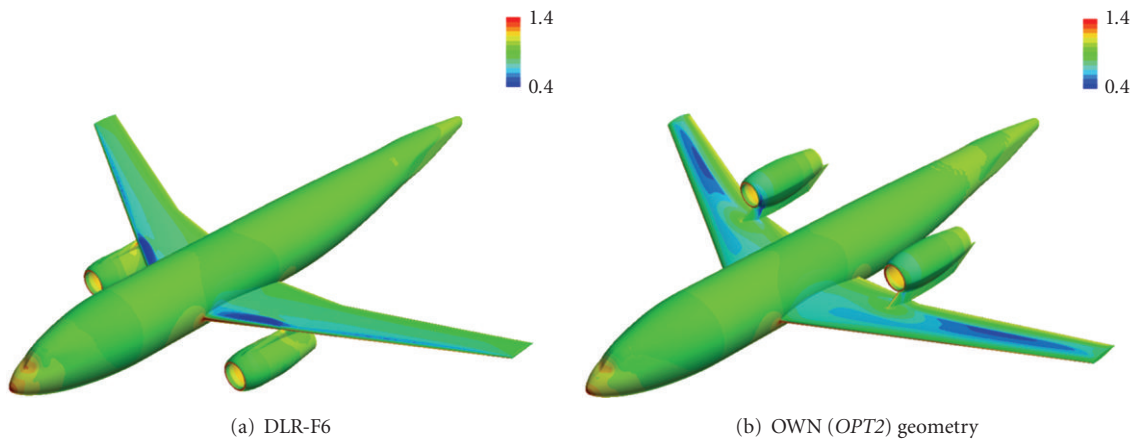


FIGURE 21: Comparison of surface pressure coefficient contours.

effect of the noise propagation toward the ground caused by fan and jet noises. By conducting further optimization integrating all the components at various flight conditions, OVN configuration will be able to prove that it is a potential candidate to be a near-future aircraft.

### 6. Conclusion

Aerodynamic optimizations of OVN configuration were conducted by modifying nacelle position, nacelle shape, wing shape, and pylon shape to investigate the usefulness of an OVN configuration. Firstly, the nacelle position and its shape as well as wing shape were optimized to maximize

$L/D$  and to achieve preferable nacelle position for a realistic aircraft design in terms of structural and maintenance points of view. As a result of the optimization, optimal configuration (*OPT1*) achieved  $L/D$  of 34.5. It reveals that the nacelle position is highly related to aerodynamic performance of OVN configuration; however, reasonable  $L/D$  can be obtained by the modification of nacelle and wing shape even when the nacelle is close to a wing.

Secondly, the pylon shape of the above optimal configuration was further optimized to reduce the interference effect between a wing and a nacelle. As a result of the optimization, the buffet near the trailing edge was weakened compared with original pylon shape. This enabled to

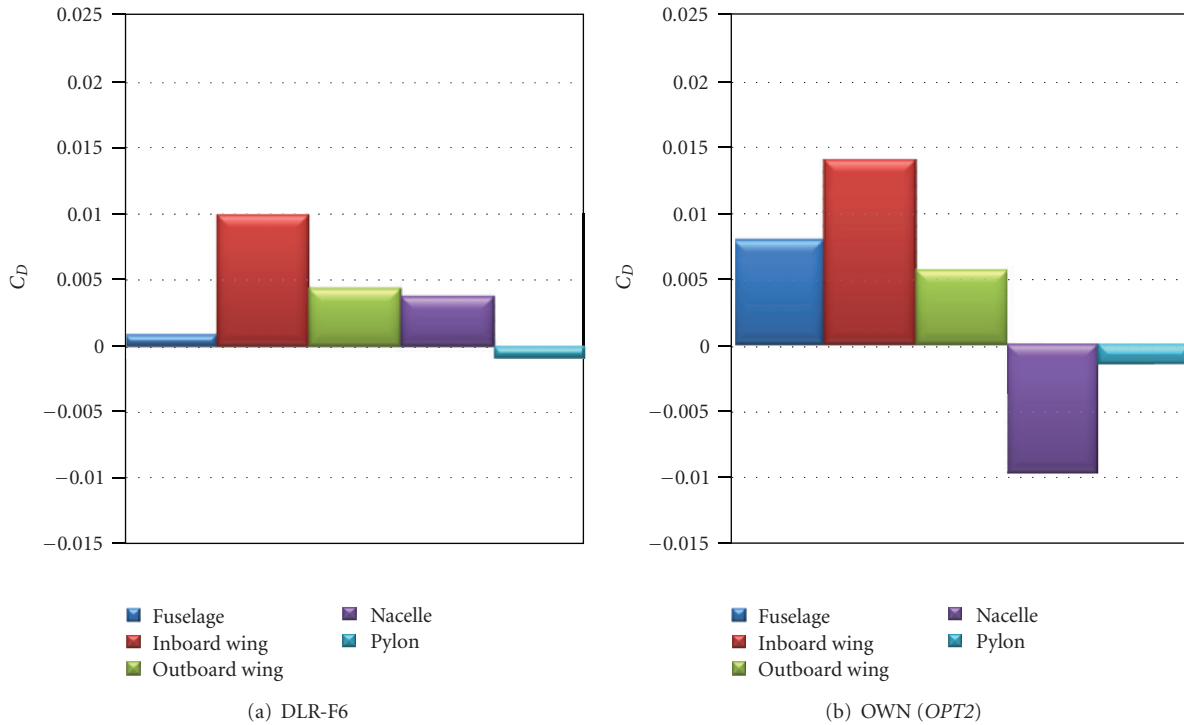


FIGURE 22: Proportion of pressure drag coefficient.

achieve higher  $L/D$  of 35.5 corresponding to 5 drag counts reduction from the first optimization. The optimal geometry (OPT2) is compared with DLR-F6 as a representative of conventional UWN. It proves that cruise performance of OWN can be comparable to that of UWN. Through the present aerodynamic optimizations of OWN configuration, it is concluded that an aerodynamically efficient OWN configuration comparable to conventional UWN will be realized feasible with further optimization under the various flight conditions and further integrated optimization of nacelle, wing, pylon and fuselage configuration.

## Acknowledgment

The present computation was executed by using NEC Vector Supercomputer of SX-9 in Cyberscience Center of Tohoku University.

## References

- [1] M. Fujino and Y. Kawamura, "Wave-drag characteristics of an over-the-wing nacelle business-jet configuration," *Journal of Aircraft*, vol. 40, no. 6, pp. 1177–1184, 2003.
- [2] J. Ricouard, R. Davy, P. Loheac, A. Moore, and O. Piccin, "ROSAS wind tunnel test campaign dedicated to unconventional aircraft concepts study," in *Proceedings of the 10th AIAA/CEAS Aeroacoustics Conference*, pp. 783–792, Manchester, UK, May 2004.
- [3] D. Sasaki and S. Obayashi, "Efficient search for trade-offs by adaptive range multi-objective genetic algorithms," *Journal of Aerospace Computing, Information and Communication*, vol. 2, no. 1, pp. 44–64, 2005.
- [4] M. Sunago, D. Sasaki, K. Takenaka, and K. Nakahashi, "Multipoint optimization of a short-range quiet passenger aircraft," *Journal of Aircraft*, vol. 46, no. 3, pp. 1070–1074, 2009.
- [5] S. Jeong, Y. Minemura, and S. Obayashi, "Optimization of combustion chamber for diesel engine using kriging model," *Journal of Fluid Science and Technology*, vol. 1, pp. 138–146, 2006.
- [6] S. Jeong, M. Murayama, and K. Yamamoto, "Efficient optimization design method using kriging model," *Journal of Aircraft*, vol. 42, no. 2, pp. 413–420, 2005.
- [7] M. D. McKay, R. J. Beckman, and W. J. Conover, "A comparison of three methods for selecting values of input variables in the analysis of output from a computer code," *Technometrics*, vol. 21, no. 2, pp. 239–245, 1979.
- [8] November 2010, <http://aaac.larc.nasa.gov/tsab/cfdlarc/aiaa-dpw/Workshop3/DPW3-geom.html>.
- [9] H. Sobieczky, "Parametric airfoils and wings," in *Notes on Numerical Fluid Mechanics*, pp. 71–88, 1998.
- [10] Y. Ito and K. Nakahashi, "Surface triangulation for polygonal models based on CAD data," *International Journal for Numerical Methods in Fluids*, vol. 39, no. 1, pp. 75–96, 2002.
- [11] D. Sharov and K. Nakahashi, "Hybrid prismatic/tetrahedral grid generation for viscous flow applications," *AIAA Journal*, vol. 36, no. 2, pp. 157–162, 1998.
- [12] K. Nakahashi, Y. Ito, and F. Togashi, "Some challenges of realistic flow simulations by unstructured grid CFD," *International Journal for Numerical Methods in Fluids*, vol. 43, no. 6-7, pp. 769–783, 2003.

- [13] S. Obayashi and G. P. Guruswamy, "Convergence acceleration of a Navier-Stokes solver for efficient static aeroelastic computations," *AIAA journal*, vol. 33, no. 6, pp. 1134–1141, 1995.
- [14] V. Venkatakrishnan, "On the accuracy of limiters and convergence to steady-state solutions," AIAA Paper 93-0880, 1992.
- [15] D. Sharov and K. Nakahashi, "Reordering of hybrid unstructured grids for lower-upper symmetric Gauss-Seidel computations," *AIAA Journal*, vol. 36, no. 3, pp. 484–486, 1998.



# Hindawi

Submit your manuscripts at  
<http://www.hindawi.com>

